Journal of Engineering Science and Technology Review 17 (6) (2024) 49-58

Research Article

JOURNAL OF
Engineering Science and Technology Review

www.jestr.org

Analysis Model and Strength Prediction Method of Wing Crack Propagation Considering Influence of Crack Inclination Angle

Yanhai Zhao[1,2,3,*], Yanyu Wang[1] and Qiang Cui[4]

[1]*School of Civil Engineering and Architecture, Northeast Electric Power University, Jilin 132012, China*
[2]*Fujian Research Center for Tunneling and Urban Underground Space Engineering, Huaqiao University, Xiamen 361021, China*
[3]*Sanming Coffer Fine Chemical Industrial Co., Ltd., Sanming 365500, China*
[4]*State Grid Electric Power Engineering Research Institute Co., Ltd., Beijing 102401, China*

Received 3 September 2024; Accepted 19 December 2024

Abstract

To investigate the deformation and failure characteristics of loaded sandstone under the influence of fracture dip angles and characterizing the propagation patterns of wing cracks in fractured rocks, the stress-strain characteristics and failure modes of sandstone samples with different fracture dip angles were analyzed through uniaxial compression tests. A wing crack propagation model in fractured rocks was established based on relevant theories of fracture mechanics. Further, a rock strength calculation method that considers the influence of fracture dip angles was proposed by combining the M-C strength criterion and the Box-Lucas1 function and validated by experimental data. Results show a close match between theoretical and experimental results. As the distance between the wing crack initiation position and the fracture end increases, the fracture dip angle increases while the wing crack initiation angle decreases first, then increases, and finally shows a single descending trend. When the fracture dip angle increases, the longitudinal difference between the peak strength curves first rises and then drops. The conclusions obtained in this study provide theoretical basis and technical support for the stability assessment and engineering application of fractured rocks.

Keywords: Fracture dip angle, Sandstone, Wing crack, Failure mode, Mechanical mechanism

1. Introduction

Throughout the extensive geological timeline spanning hundreds of millions of years, a multitude of fractures have naturally developed within rock formations. The inherent variability and the discontinuities within these rocks substantially influence their mechanical behavior [1, 2]. In numerous engineering applications, including tunnel construction, rock slope stability assessments, and the design of support systems in underground mining, a critical need arises to forecast the strength and failure properties of fractured rock formations. Moreover, the inevitability of dealing with the propagation of fractures within rock bodies arises during excavation activities. Therefore, it is crucial to scrutinize the processes governing crack propagation in fractured rocks and their influence on the deformation and fracturing patterns of the rock [3]. Concurrently, the behaviors of crack initiation, spread, and eventual failure are subjects of significant interest among engineering professionals and researchers alike.

Fracture of rock mass has significant influence on engineering stability. In order to ensure the safe and stable operation of the project, it is necessary to fully consider the factors of rock fracture during the site selection, design, construction and long-term operation of the project. By adopting effective engineering measures and monitoring means, the influence of crack on engineering stability can be reduced, and the safety and reliability of engineering can be improved [4]. In the practice of many geotechnical engineering, such as the excavation of roadway and highway and railway tunnel, the stability analysis of rock slope, and the design of pillar in deep mining, it is usually necessary to analyze the strength and fracture propagation characteristics of natural rock mass containing various joints and fractures under the influence of construction disturbance [5, 6]. Currently, there is a lack of sophisticated models for calculating the propagation angle and length of wing cracks, as well as a deficiency in rock strength calculation methods that account for the influence of crack inclination [7, 8].

In underground engineering, the stability of fractured rocks is crucial to construction safety. The randomness of fracture dip angles in the rock leads to the generation of wing cracks with different geometric shapes when the rock is loaded. The propagation of wing cracks can not only alter the stress state within the rock but also may deteriorate the rock's local or overall mechanical properties, such as strength and stiffness, ultimately causing deformation and fracture of the rock [9]. Therefore, probing into the propagation mechanism of wing cracks in fractured rocks can better address the issue of rock stability in underground engineering, thereby ensuring the safety and reliability of engineering structures.

2. State of the art

In recent years, many scholars have explored the propagation mechanism of rock wing crack and its influence on rock failure mode by means of experimental research, theoretical analysis and modeling. In terms of experimental research, various scholars used different test techniques to analyze the evolution characteristics of cracks in loaded rock

*E-mail address: qingtingnbai@163.com
ISSN: 1791-2377
doi:10.25103/jestr.176.07

samples [10, 11]. Wong and Xiong [12] were the first to achieve the quantitative and continuous analysis of mesoscale and macroscale fracture processes through uniaxial compression tests conducted on marble specimens that contained precast cracks. Yang and Jing [13] conducted the study on the failure under strength and the behavior of crack propagation in sandstone with a single fracture. They also assessed the impact of the fracture's length and inclination on various aspects, including the stone's strength and deformation properties, the distribution of acoustic emissions (AE), and the mechanisms involved in the propagation of cracks within the sandstone. Naderloo et al. [14] used the two-dimensional AE source location method and the new algorithm to locate the crack initiation and expansion path in the loaded sample, indicating that the acoustic emission method can accurately predict the damage location and its mechanism. However, in the actual engineering practice, the application of these detection techniques is often limited by the site construction conditions and cannot participate in the measurement, so it is very important to use the theoretical model to predict and analyze the crack propagation mode in the rock mass.

In the use of relevant theories for analysis, Bernabe and Pec [15] introduced the concept of micro-shear zones to elucidate how wing crack propagation affects rock creep and the failure process. Duriez et al. [16] used discrete element method to simulate crack propagation of open and closed defects and studied the microscopic damage mechanism in the process of wing crack propagation. Lee et al. [17] used phase field model to study the formation mechanism of wing crack. Pepe et al. [18] conducted a comprehensive analysis of mechanical parameter data from over 480 unconfined compression tests on intact rocks, employing both single and multiple regression techniques. Through this analysis, they established the correlation between key mechanical attributes of the rocks and the stress thresholds at which cracking initiates.

In the establishment of model research, Mohammadi and Pietruszczak [19] formulated a model that describes the failure process in pre-cracked rock specimens, and elaborated on the intricate fracture patterns associated with the emergence and spread of new cracks within these pre-existing zones. Dang-Trung et al. [20] constructed a wing crack propagation model grounded in linear elastic fracture mechanics, taking into account fracture contact mechanics, to investigate the genesis and progression of wing cracks during shearing. Mohanty and Das [21] applied 3D finite element analysis to study the onset and growth of wing cracks in sandstone, using the VCCT (virtual crack closure technology) and the stress/strain-based LEFM (linear elastic fracture mechanics) for embedded crack evaluation. Yang et al. [22] performed uniaxial compression tests to evaluate the impact of wing cracks on rock mechanics and developed computational models to predict both wing crack paths and rock strength. They conducted the dynamics of wing crack propagation in depth.

In this study, the mechanical characteristics of fractured rock under load and the failure mode under uniaxial compression were summarized by analyzing the uniaxial compression test results of fractured red sandstone. Based on the theory of fracture mechanics, the propagation model of airfoil crack was established. By analyzing the data with Box-Lucas1, a calculation method of rock strength considering the influence of fracture dip angle was also proposed. In addition, the mechanical relationship between wing crack propagation and progressive rock failure was analyzed by introducing wing crack propagation factor. The results obtained are crucial in deciphering the mechanisms of deformation and fracturing in rock, as well as in enhancing the stability and safety analysis within the realm of rock mass engineering.

The rest of this study is organized as follows: In Section 3, the uniaxial compression tests are carried out on red sandstone with prefabricated fractures, focusing on the influence of the inclination angle of the fracture in the rock on its mechanical behavior under load and failure mode. In Section 4, a wing crack propagation model of fractured rock is constructed, and a rock strength calculation method considering the influence of crack inclination is also proposed. Furthermore, a wing crack propagation factor is incorporated to elucidate the mechanisms of deformation and fracturing in loaded cracked rock. The conclusions are summarized in Section 5.

3. Methodology

3.1 Experimental materials

Red sandstone with a granular clastic texture was selected for uniaxial compression tests. According to lithology and disintegration properties, it belongs to the third category of red sandstone, and its non-disintegration characteristics are indistinguishable from ordinary sandstone. The predominant clastic minerals are quartz, felspar, and calcite, accompanied by minor hematite and mica. The clay minerals comprise montmorillonite, illite, kaolinite, and chlorite. To prevent inherent defects in the rock samples from affecting the test results, a careful inspection was made of the appearance of the samples, ensuring that there were no visible joint cracks, and no significant differences among the various specimens.

3.2 Experimental materials

According to the requirements of the International Society for Rock Mechanics and Rock Engineering (ISRM), the samples were processed into standard cylindrical specimens with dimensions of Φ 50 mm × 100 mm. Fig. 1 shows a schematic diagram of the prefabricated fractured specimens, where the fracture length was 20 mm, the fracture width was 2 mm, and the fracture dip angle was β (i.e., the angle between the fracture and the horizontal direction). The fractures were cut using a water jet, and three fracture dip angles of 30°, 60°, and 90° were set.

3.3 Test system and loading process

The diameter of the rock sample is 50 mm, the height is 100 mm, and the whole is a standard cylinder. Fig. 1 depicts these specimens with prefabricated fractures, characterized by a 20 mm fracture length, 2 mm width, and a dip angle β, indicating the fracture's slope in relation to the horizontal. These fractures were precisely cut using a water jet method, resulting in three different dip angles: 30°, 60°, and 90°.

The RMT-150B hydraulic loading testing machine is used in this experiment (Fig. 2). The maximum load of the vertical hydraulic cylinder is 1000 kN, and the loading rate range is 0.01-100 kN/s. The instrumentation for the uniaxial compression tests comprised a 1000 kN load cell to measure the vertical force, a 5 mm displacement sensor for vertical deformation, and two 2.5 mm displacement sensors for horizontal deformation. The testing sequence began with securing the specimen with rubber bands, followed by placing rigid pads on both ends to minimize end effects on the test outcomes and zeroing the sensors. Finally, using the

control platform software to control the displacement rate at 0.01 mm/s, the fractured red sandstone samples are loaded to complete failure. Specimens of each inclination angle are tested five times in accordance with the steps described above. The resulting data are recorded and their average values are taken to determine the relevant physical and mechanical parameters and stress-strain characteristics of the test sample.

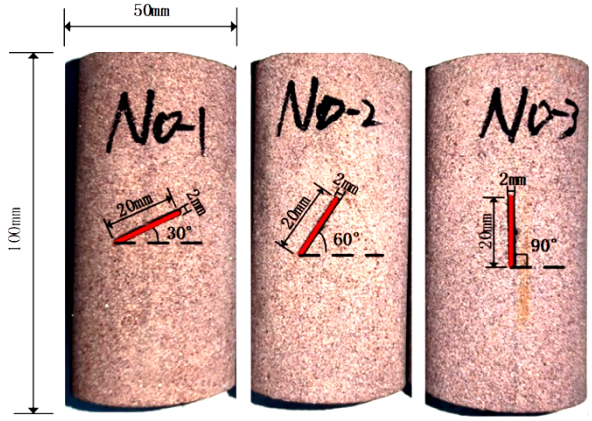

Fig. 1. Schematic diagram of prefabricated fractured specimen

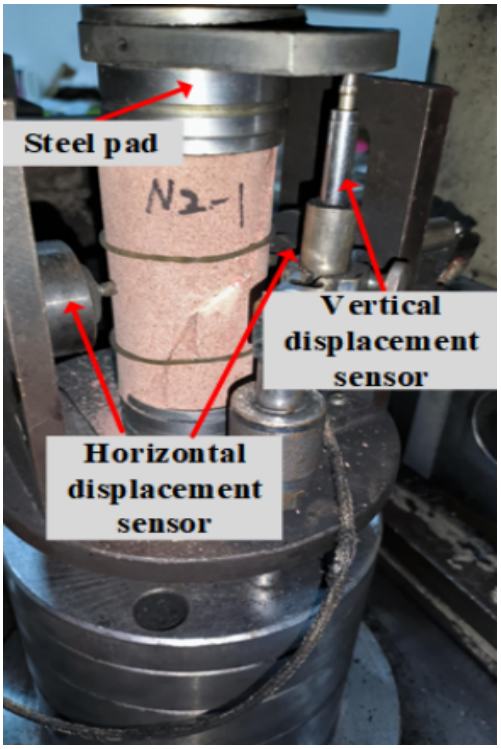

Fig. 2 Schematic diagram of the test system

4. Results analysis and discussion

4.1 Deformation and failure characteristics of rock with different fracture dip angles

Fig. 3(a) displays the mean stress-strain behavior for Group N0 rock samples subjected to uniaxial compression, highlighting the impact of varying fracture dip angles. The intact samples exhibited higher characteristic strengths than the fractured ones. Notably, samples with a 90° fracture dip angle had strength values more similar to intact samples than those with other angles. The stress-strain curve's division identified the closure point, where the slope began to rise and then stabilized, indicating the closure of microfractures under axial stress. The point at which the stress-strain curve's slope shifted from stable to a gradual decline was identified as the onset of crack initiation, marking the emergence of wing cracks along the rock's fractures. Ordinate extremum points on the curve characteristics of maximum stress and the ultimate bearing capacity of the rock.

Analysis of samples with three distinct fracture dip angles revealed that the slope of the compaction-stage curve, which is the section between the initiation and closure points on the stress-strain curve, steepened with an increasing fracture dip angle. This increase was due to the reduced projection of the fracture on the cross-section at higher angles, which intensified the axial stress's compaction on lateral microfractures and heightened the rock's stiffness. Consequently, as axial stress increased, the specimens displayed increased stiffness in the elastic stage, prolonging this phase and deferring crack formation. Finally, the occurrence of the above situation results in the change rule of the maximum strength corresponding to rocks with different fracture dip angles as described above.

Fig. 3(b) shows that the three key stresses increased as the fracture dip angle rose. This pattern suggests that a higher fracture dip angle reduces the fracture's projected length on the cross-section, diminishing its impact on the specimen's mechanical properties.

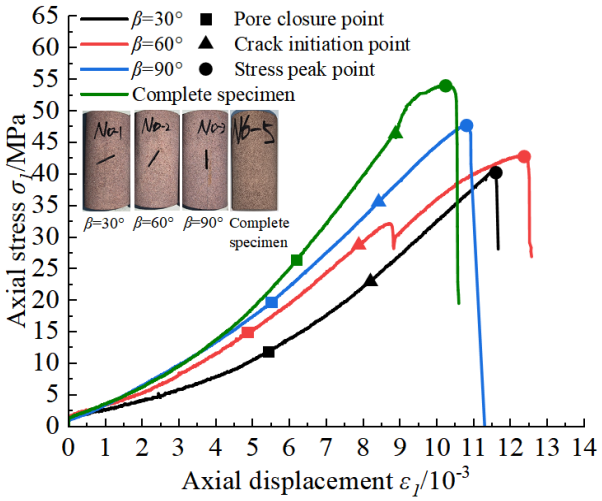

(a) Stress-strain curves of specimens with different fracture dip angles

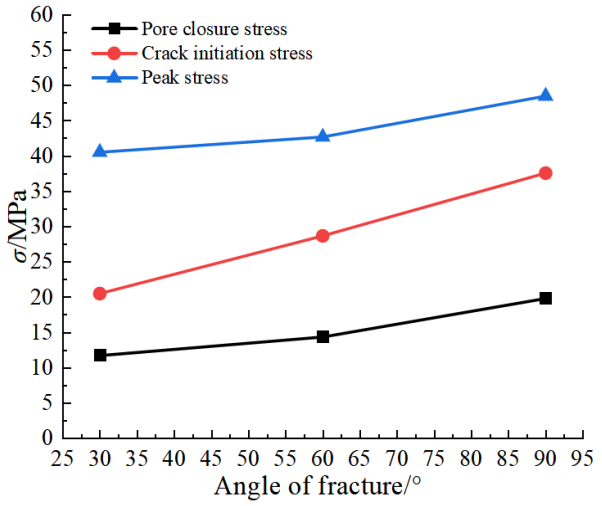

(b) Stress curves of specimens with different fracture dip angles

Fig. 3. Stress-strain and characteristic stress curves of specimens with different fracture dip angles under uniaxial compression

The left part of Fig. 4 shows the samples after failure, the middle part shows sketches of the fractures, and the right part presents a schematic diagram of the distribution of wing cracks after simplifying to a theoretical model. The red lines in the sketches represent prefabricated fractures. The aforementioned Fig. 4 depicts the macroscopic fracture patterns in the specimens following failure under uniaxial compression: At a rock fracture inclination of 30°, shear wing cracks emerge at the fracture's terminus post-loading, while tensile reverse wing cracks develop in the location opposite to their propagation direction. The failure mode of the specimen at this stage was characterized as a tensile fracture. At a prefabricated fracture angle of 60°, the specimen's failure was marked by a shear crack that extended across the pre-existing fracture. At the 60° prefabricated fracture angle, a wing crack emanated from one end of the through-going shear crack and propagated towards the specimen's end, resulting in the spalling of rock particles around the crack. This scenario corresponds to a single-oblique shear failure mode. At a 90° prefabricated fracture angle, the main crack took the form of a tensile crack that traversed the prefabricated fracture. Several distinct wing-shaped cracks emerged at the terminus of the primary crack's propagation path, and the emergence of these cracks resulted in the extensive shedding of rock particles beyond the sample's boundaries. Upon the crack angle attaining 90°, the specimen experiences a fracture failure mode under compressive loading. Investigations into the fracture behaviors of samples under uniaxial compression, across a spectrum of fracture angles, reveal that the angle of the fracture is a critical determinant of the overall mode of failure and the path that cracks take under load. The progression of the main crack's expansion alternates between tensile and shear mechanisms, ultimately returning to a tensile state. As the fracture angle increases, the rock's failure pattern transitions from tensile to monoclinic shear, culminating in a complete fracture failure.

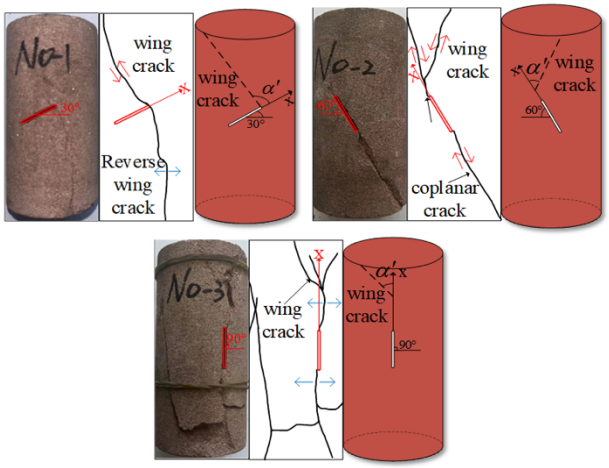

Fig. 4. Failure modes of sandstone with different fracture dip angles under uniaxial compression

4.2 Wing crack propagation analysis model considering influence of fracture dip angles

4.2.1 Establishment of wing crack propagation analysis model

Upon loading, the propagation of wing cracks within fractured rock substantially influences the stress-strain characteristics of the rock sample. These wing cracks, as they extend around the main fracture, alter the stress distribution, thereby affecting the specimen's mode of failure. In addition to the above effects, this fracture parameter has a significant effect on the initiation and propagation of wing cracks. Fig. 5 below shows the schematic diagram of the mechanical model obtained after the mechanical simplification of the fractured rock in this study. The purpose of this model is to use for mechanical analysis to obtain the winglike crack propagation mode of the rock with its own fractures under external load or construction disturbance. The model describes the propagation and splitting behavior of winglike cracks in loaded rock from a quantitative perspective, and discusses the effects of the propagation of these cracks on the strength and failure characteristics of rock itself.

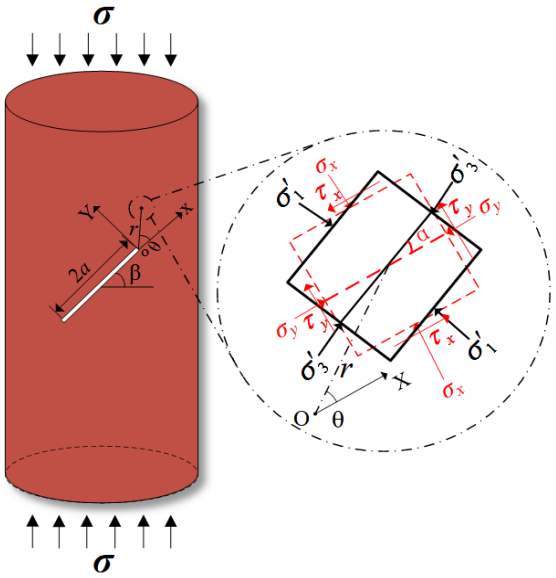

Fig. 5 Wing crack propagation model for fractured rock

Within this framework, the cylindrical structure emblematizes the rock that has experienced fracturing. Uniform axial stress, denoted by σ, was applied uniformly across the top and bottom surfaces of the cylinder. Positioned at the core of the cylinder, an all-passing fissure spanned a length of $2a$ and intersected the horizontal plane at an angle β. Taking the center of the prefabricated fracture as the original point, a polar coordinate system X-Y was established as shown in Fig. 5.

A unit element was taken at point (r, θ) near the end of the fracture, and enlarged as shown in the right part of Fig. 5. The presence of a fracture in the specimen induces a specific stress state in the unit element within the X-Y coordinate system, which corresponds to the stress state of the red unit element under axial stress application to the specimen. The black unit element represents the principal stress distribution state of this unit element. As the axial stress gradually rose, failure occurred when the Mohr's circle of its principal stress was tangent to the strength envelope line, according to the Mohr-Coulomb (M-C) strength theory. As known from observations of wing crack initiation points on the specimen after failure, these points were all near the top side of the fracture end. Hence, it was assumed that the initiation point of the wing crack in this model was at point (1, 90) in the X-Y coordinate system. Wing cracks began to appear when the principal stress at this point reached its ultimate state.

By referring to the relevant theories of fracture mechanics, the problem of wing crack propagation is approximated as the problem of I-II type combined crack under stress state in the physical model established above.

For the mixed-mode I-II fracture issue, the Westergaard stress function was employed to determine the stress intensity factors, as detailed subsequently:

$$\left.\begin{aligned} K_{\mathrm{I}} &= \sigma\sqrt{\pi a}\sin^2\beta \\ K_{\mathrm{II}} &= \frac{\sigma\sqrt{\pi a}}{2}\sin 2\beta \end{aligned}\right\} \tag{1}$$

Stress distributions in the vicinity of the precrack tip can be derived by integrating the stress components associated with Mode I and Mode II:

$$\left.\begin{aligned} \sigma_x &= \frac{K_{\mathrm{I}}}{\sqrt{2\pi r}}\cos\frac{\theta}{2}\left(1-\sin\frac{\theta}{2}\sin\frac{3\theta}{2}\right) \\ &-\frac{K_{\mathrm{II}}}{\sqrt{2\pi r}}\sin\frac{\theta}{2}\left(2+\cos\frac{\theta}{2}\cos\frac{3\theta}{2}\right) \\ \sigma_y &= \frac{K_{\mathrm{I}}}{\sqrt{2\pi r}}\cos\frac{\theta}{2}\left(1+\sin\frac{\theta}{2}\sin\frac{3\theta}{2}\right) \\ &+\frac{K_{\mathrm{II}}}{\sqrt{2\pi r}}\sin\frac{\theta}{2}\cos\frac{\theta}{2}\cos\frac{3\theta}{2} \\ \tau_{xy} &= \frac{K_{\mathrm{I}}}{\sqrt{2\pi r}}\sin\frac{\theta}{2}\cos\frac{\theta}{2}\cos\frac{3\theta}{2} \\ &+\frac{K_{\mathrm{II}}}{\sqrt{2\pi r}}\cos\frac{\theta}{2}\left(1-\sin\frac{\theta}{2}\sin\frac{3\theta}{2}\right) \end{aligned}\right\} \tag{2}$$

At this time, the magnitudes σ_1 and σ_3 and direction angle α_0 of the principal stresses on the principal-stress unit element at this point were:

$$\left.\begin{aligned} \sigma_1 &= \frac{\sigma_x+\sigma_y}{2}+\sqrt{\left(\frac{\sigma_x-\sigma_y}{2}\right)^2+\tau_{xy}^2} \\ \sigma_3 &= \frac{\sigma_x+\sigma_y}{2}-\sqrt{\left(\frac{\sigma_x-\sigma_y}{2}\right)^2+\tau_{xy}^2} \\ \alpha_0 &= -\frac{1}{2}\arctan\frac{2\tau_{xy}}{\sigma_x-\sigma_y} \end{aligned}\right\} \tag{3}$$

By substituting Eq. (2) into Eq. (3), we obtained the following results:

$$\left.\begin{aligned} \sigma_1 &= \frac{K_{\mathrm{I}}}{\sqrt{2\pi r}}\cos\frac{\theta}{2}-\frac{K_{\mathrm{II}}}{\sqrt{2\pi r}}\sin\frac{\theta}{2} \\ &+\sqrt{\left(\frac{AK_{\mathrm{I}}}{\sqrt{2\pi r}}+\frac{2K_{\mathrm{II}}}{\sqrt{2\pi r}}\sin\frac{\theta}{2}+\frac{BK_{\mathrm{II}}}{\sqrt{2\pi r}}\right)^2+\left(\frac{BK_{\mathrm{I}}}{\sqrt{2\pi r}}+\frac{K_{\mathrm{II}}}{\sqrt{2\pi r}}\cos\frac{\theta}{2}-\frac{AK_{\mathrm{II}}}{\sqrt{2\pi r}}\right)^2} \\ \sigma_3 &= \frac{K_{\mathrm{I}}}{\sqrt{2\pi r}}\cos\frac{\theta}{2}-\frac{K_{\mathrm{II}}}{\sqrt{2\pi r}}\sin\frac{\theta}{2} \\ &-\sqrt{\left(\frac{AK_{\mathrm{I}}}{\sqrt{2\pi r}}+\frac{2K_{\mathrm{II}}}{\sqrt{2\pi r}}\sin\frac{\theta}{2}+\frac{BK_{\mathrm{II}}}{\sqrt{2\pi r}}\right)^2+\left(\frac{BK_{\mathrm{I}}}{\sqrt{2\pi r}}+\frac{K_{\mathrm{II}}}{\sqrt{2\pi r}}\cos\frac{\theta}{2}-\frac{AK_{\mathrm{II}}}{\sqrt{2\pi r}}\right)^2} \\ \alpha_0 &= \frac{1}{2}\arctan\left(\frac{BK_{\mathrm{I}}+K_{\mathrm{II}}\cos\frac{\theta}{2}-AK_{\mathrm{II}}}{AK_{\mathrm{I}}+2K_{\mathrm{II}}\sin\frac{\theta}{2}+BK_{\mathrm{II}}}\right) \end{aligned}\right\} \tag{4}$$

where,

$$\left.\begin{aligned} A &= \cos\frac{\theta}{2}\sin\frac{\theta}{2}\sin\frac{3\theta}{2} \\ B &= \sin\frac{\theta}{2}\cos\frac{\theta}{2}\cos\frac{3\theta}{2} \end{aligned}\right\} \tag{5}$$

According to the M-C strength criterion, when the location near the fracture end is under ultimate stress, Mohr's stress circle at this location is tangent to the rock strength envelope line $\tau = c-\sigma\tan\varphi$, where c is the cohesive force of the rock, and φ is the internal friction angle of the rock. The Mohr circle is connected to the center of the circle at the point tangent to the rock strength envelope. The angle of the tangent line formed by the connection point and the coordinate axis is twice the angle of the fracture plane and the maximum principal stress plane. In this model, the macroscopic wing crack has an angle of α' with the positive X-axis of the polar coordinate system:

$$\alpha' = 45^{\circ}+\frac{\varphi}{2}+|\alpha_0| \tag{6}$$

When subjected to external loads, fractured samples form a plastic zone in the vicinity of the crack tip, which is notably small in rock materials-significantly smaller than both the pre-existing fracture and the specimen itself. As the material at the crack tip deforms plastically, wing cracks begin and extend. By taking into account the relative displacement between the initiation and propagation plane of the wing crack, the crack tip displacement theory enables us to determine the propagation length δ of the wing crack as follows:

$$\delta = 2\sqrt{u^2+v^2} \tag{7}$$

where u represents the displacement of the wing crack along the X-direction, and v represents the displacement of the wing crack along the Y-direction.

Through the comprehensive analysis of the above M-C strength criterion and the displacement field theory of fracture mechanics, the final propagation length of the wing crack germinated near the end of the crack initiation position can be transformed into the problem of solving the displacement field of the I-II complex crack at the end of the crack propagation in fracture mechanics by reasonable optimization. To solve the above problems in fracture mechanics:

$$\left.\begin{aligned} u &= \frac{2}{E}\sqrt{\frac{r}{2\pi}}\left\{\begin{aligned} &K_{\mathrm{I}}\cos\frac{\theta}{2}\left[(1-\upsilon)+(1+\upsilon)\sin^2\frac{\theta}{2}\right] \\ &+K_{\mathrm{II}}\sin\frac{\theta}{2}\left[(1+\upsilon)\cos^2\frac{\theta}{2}+2\right] \end{aligned}\right\} \\ v &= \frac{2}{E}\sqrt{\frac{r}{2\pi}}\left\{\begin{aligned} &K_{\mathrm{I}}\sin\frac{\theta}{2}\left[(1-\upsilon)+(1+\upsilon)\sin^2\frac{\theta}{2}\right] \\ &+K_{\mathrm{II}}\cos\frac{\theta}{2}\left[(1+\upsilon)\sin^2\frac{\theta}{2}-(1-\upsilon)\right] \end{aligned}\right\} \end{aligned}\right\} \tag{8}$$

where, υ is Poisson's ratio; r is the radius of the plastic zone.

$$r = \frac{1}{2\pi\sigma_W^2}\left(b_{11}K_{\mathrm{I}}^2+b_{12}K_{\mathrm{I}}K_{\mathrm{II}}+b_{22}K_{\mathrm{II}}^2\right) \tag{9}$$

At this point, the stress intensity factors were:

$$\left.\begin{aligned} K_{\mathrm{I}} &= \sigma_W \sqrt{\pi a}\sin^2\beta \\ K_{\mathrm{II}} &= \frac{\sigma_W \sqrt{\pi a}}{2}\sin 2\beta \end{aligned}\right\} \tag{10}$$

$$\sigma_W = \sigma - \sigma_a \tag{11}$$

where, σ_a is the crack initiation stress

$$\left.\begin{aligned} b_{11} &= \cos^2\frac{\theta}{2}\left(3M^2+1\right)+3N^2\sin^2\frac{\theta}{2} \\ b_{12} &= 2\sin\frac{\theta}{2}\cos\frac{\theta}{2}\left(3M+3N-1\right) \\ b_{22} &= \sin^2\frac{\theta}{2}\left(4+6N+3N^2\right)+3\cos^2\frac{\theta}{2}\left(1-M\right)^2 \end{aligned}\right\} \tag{12}$$

$$\left.\begin{aligned} M &= \sin\frac{\theta}{2}\sin\frac{3\theta}{2} \\ N &= \cos\frac{\theta}{2}\cos\frac{3\theta}{2} \end{aligned}\right\} \tag{13}$$

4.2.2 Rock strength analysis based on wing crack propagation model

In order to more accurately analyze the failure state of rocks with different fracture dip angles under uniaxial load through quantitative analysis mode, this study innovatively introduces the wing crack propagation coefficient λ. This factor is characterized as the proportion of the vertical projection length $L_0$of the wing crack to the length L projected from the crack initiation point to the specimen's top surface. As depicted in the accompanying figure.

$$\lambda = \frac{L_0}{L} \tag{14}$$

Fig. 6 is a schematic diagram for calculating the wing crack propagation factor in fractured rock. Using the wing crack propagation length obtained from the previous section, we calculated and obtained L and L_0. Then substituted them into Eq. (14), obtaining λ.

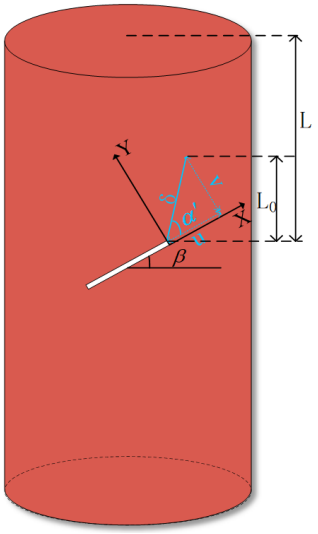

Fig. 6. Schematic diagram for calculating the wing crack propagation factor in fractured rock

Fig. 6 referenced previously illustrates a methodological diagram for assessing the wing crack propagation coefficient in rock formations with fractures. Utilizing the wing crack propagation distance obtained from the earlier section, we calculated the values for L and L_0. These computed values were then substituted into Eq. (14) to determine the λ factor.

Based on the wing crack propagation model and combined with the M-C strength theory, the strength of fractured rock was calculated. According to the M-C strength criterion:

$$\sin\varphi = \frac{\sigma_1 - \sigma_3}{\sigma_1 + \sigma_3 + 2c\cot\varphi} \tag{15}$$

By combining Eq. (4) with Eq. (15), we obtained:

$$\begin{aligned} &\left(A^2+B^2-\frac{\sin^2\varphi}{2}\right)K_{\mathrm{I}}{}^2+\left(\frac{5}{2}+A^2-\sqrt{2}A+2\sqrt{2}B-\frac{\sin^2\varphi}{2}\right)K_{\mathrm{II}}{}^2 \\ &+\left(2\sqrt{2}A+\sqrt{2}B+\sin^2\varphi\right)K_{\mathrm{I}}K_{\mathrm{II}} \\ &-2\sqrt{\pi}c\sin\varphi\cos\varphi\left(K_{\mathrm{I}}-K_{\mathrm{II}}\right)-2\pi c^2\cos^2\varphi=0 \end{aligned} \tag{16}$$

After substituting Eq. (1) into Eq. (16), we obtained Eq. (17). Eq. (17) can be solved by substituting relevant parameters. Further, a rock strength calculation method was proposed for this model considering that the theoretical value calculated here for this model was the stress experienced when a wing crack initiated locally.

$$\begin{aligned} &10\pi\sin^4\beta\left(A^2+B^2-\frac{\sin^2\varphi}{2}\right)\sigma^2 \\ &+\frac{5\pi}{2}\sin^2 2\beta\left(\frac{5}{2}+A^2-\sqrt{2}A+2\sqrt{2}B-\frac{\sin^2\varphi}{2}\right)\sigma^2 \\ &+5\pi\sin^2\beta\sin 2\beta\left(2\sqrt{2}A+\sqrt{2}B+\sin^2\varphi\right)\sigma^2 \\ &-2\pi\sqrt{10}c\sin\varphi\cos\varphi\left(\sin^2\beta-\frac{\sin 2\beta}{2}\right)\sigma-2\pi c^2\cos^2\varphi=0 \end{aligned} \tag{17}$$

The cracking strength at the fracture end approximately exhibited an exponential function relationship with the compressive strength of the specimen, and its variation pattern conformed to the Box-Lucas1 function model. This function model is often used for fitting and constructing stress transfer relationships and constitutive relationships. [23, 24] By further processing this function model, we derived a theoretical strength calculation method:

$$\sigma_c = \kappa\left(1-e^{-\lambda\sigma}\right) \tag{18}$$

where, κ is the strength correction factor valued from 50 to 100, which was obtained through fitting; γ is the fracture length coefficient, $\gamma = 1-\frac{2a}{L}$ (where a is the half-length of the fracture and L is the height of the specimen), valued from 0 to 1.

4.3 Theoretical model analysis and influence of fracture dip angle on wing crack propagation patterns

4.3.1 Theoretical model analysis of wing crack propagation patterns

After conducting compression tests on the damaged specimens, the expansion angle of the wing crack in relation to the fracture extension line, denoted as α' in Fig. 4, was determined. As the inclination angle of the fractured rock increases from 30° to 90°, the corresponding crack propagation angles of the rock with different fracture inclination angles are 62.3°, 69.2° and 85.2°, respectively. From the above two data changes, it can be concluded that the crack inclination angle and the crack propagation angle show a positive correlation.

The ultimate stress condition at the fracture's endpoint was determined using parameters r=1, θ=0°, and a=10, along with inserting the experimentally obtained friction angles and cohesive forces into the equations to calculate the wing crack propagation angles for fractures with a variety of dip angles. The findings showed that the initial crack propagation angle $\alpha_0$decreased as the fracture dip angle increased. The relative error between the actual and calculated crack propagation angles α' was 3.89% for a 30° fracture dip angle, markedly reduced to 0.04% for a 60° angle, and was 2.40% for a 90° angle, demonstrating a high level of precision. Relevant experimental data were obtained from experiments similar to those carried out by other scholars [25-27], the wing crack propagation model is further verified. The accuracy of the model and its ability to describe the propagation characteristics of wing cracks in rocks with different fracture inclination angles are verified by comparison.

Based on the interplay between the curve and the scattered data points depicted in Fig. 7, it is evident that the wing crack growth model developed can determine the wing crack growth angle within fractured rocks with a high degree of accuracy, and the discrepancies between the calculated outcomes and experimental data are minimal. This validation underscores the model's proficiency in accurately capturing the propagation dynamics of wing cracks within the intricate structure of fractured rocks.

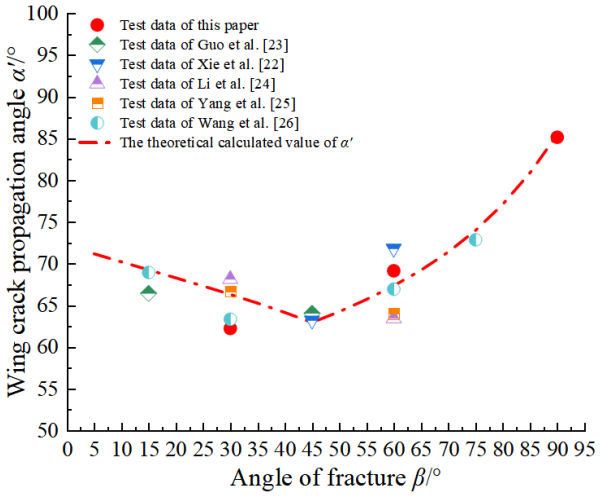

Fig. 7. Relationship curves between fracture dip angles and crack propagation angles

Additionally, the propagation angle of the crack can act as a determinant of the rock's failure mode. Combined with the rock failure mode shown in Fig. 8, it was found that the rock experienced the following failure as the fracture dip angle β increased gradually: initially, the wing crack propagation angle formed an acute angle of 72° with the crack extension line (namely a wing crack dip angle resulting in tensile failure). As that angle gradually decreased to 60°, shear wing cracks formed, leading to shear failure of the rock. Subsequently, that angle heightened to 88° again, at which time vertical wing cracks almost in the same direction as the principal stress formed, causing splitting failure of the rock. This finding also demonstrated that the failure modes of rocks can be well described using this model.

The radius r of the plastic zone was calculated by substituting the crack initiation stress σ_a, fracture dip angle β, fracture length a, and crack initiation position angle θ into Eqs. (9) to (13). Then, the obtained r was substituted into Eq. (8) to calculate the displacements u along the X-direction and v along the Y-direction of the wing crack. Further, u and v were substituted into Eq. (7), obtaining the length of a wing crack that appeared due to a fixed fracture dip angle under different axial stresses.

For crack inclinations of 30°, 60°, and 90°, the discrepancies between the theoretical predictions and experimental findings are 4.14%, 4.24%, and 3.81%, respectively. An examination of the curve's gradient indicates that the rock specimen with a 30° crack inclination exhibits the highest rate of wing crack propagation. A review of the extreme points reveals that the rock sample with a 60° crack inclination possesses the maximum wing crack length. Furthermore, the experimental values obtained by other scholars [13, 25] in uniaxial compression tests of rocks are compared with the theoretical values calculated by the model. By comparing the results, it can be seen that the theoretical values calculated by the theoretical model are consistent with the uniaxial compression test data of other scholars, and the wing crack propagation model can accurately and clearly describe the initiation and development of rock wing cracks at different fracture inclination angles.

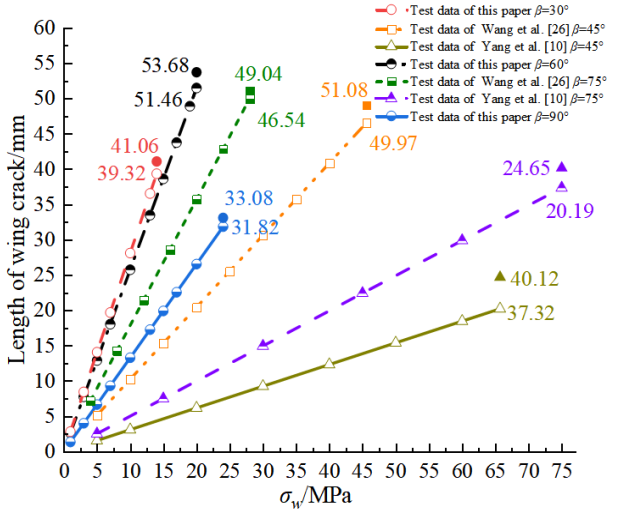

Fig. 8. Wing crack length-stress curves for fractures with different dip angles

Fig. 9 shows the variations in stress-strain characteristics and the stress-wing crack propagation factor for specimens undergoing uniaxial compression across a range of fracture dip angles. The curv's pivotal points-the commencement of wing cracking and the peak stress-align with the onset and termination of the λ-σ_1 curve, respectively, highlighting the correlation between wing crack propagation and rock failure. Under compressive loads, the specimen's macroscopic damage, quantified by the wing crack length, accumulates until it culminates in catastrophic failure. Ordinate

extremum points from the starting point to the curve, the gradient curve, namely specimen rigidity, reduce gradually, indicating a reduction in the rock's load-bearing capability with escalating stress. Moreover, the impact of macroscopic damage on this load-bearing capacity first increases and then declines as the fracture dip angle augments.

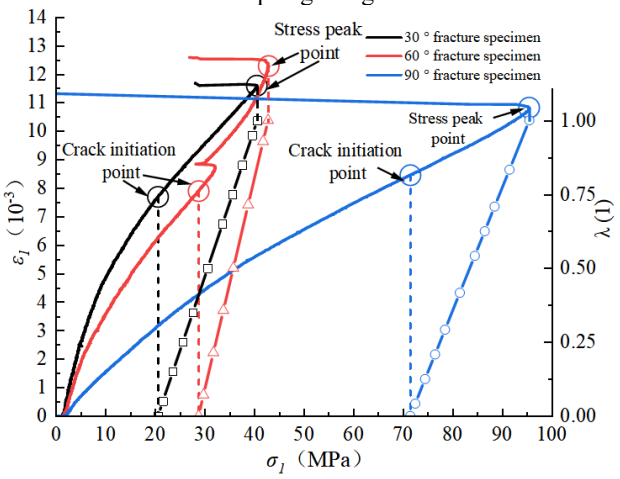

Fig. 9. Stress vs. strain curve and stress vs. wing crack propagation factor curve for specimens with different fracture dip angles under uniaxial compression

Information comprising cohesive force c and internal friction angle φ, derived from uniaxial compression tests on fractured red sandstone conducted by some researchers [26-28], was fed into the computation technique for determining the strength of fractured rock. This technique established the strength ratio as the ratio of the computed strength of the rock with fractures to that of a non-damaged sample. From the dense distribution of relevant data points in Fig. 10 beside the theoretical calculation curve in this paper, it can be intuitively inferred that there is very little gap between the prediction of rock strength by using the calculation method proposed in this paper and the actual test value under such conditions. This indicated that the proposed calculation method was highly reliable and accurate for predicting the peak strength of fractured rocks.

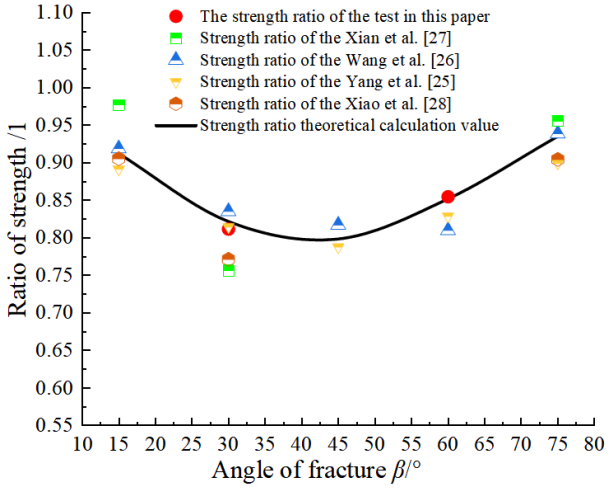

Fig. 10. Relationship curve between fracture dip angle and experimental strength of the rock

4.3.2 Influence of fracture dip angle on wing crack propagation patterns

By inserting various fracture lengths a and fracture dip angles β into Eq. (10), we derived the stress intensity factors $K_{\mathrm{I}}$and $K_{\mathrm{II}}$for specimens featuring diverse fracture lengths and dip angles. Subsequently, these computed values were employed in Eq. (10) to ascertain the radius of the plastic zone, denoted as r. This r value was then incorporated into Eq. (8) to calculate the displacements u and v in the respective X- and Y-directions of the wing crack. Ultimately, the values of u and v were fed into Eq. (7) to determine the wing crack propagation lengths, δ, in rocks exhibiting a range of fracture lengths and dip angles.

Fig. 11 presents a diagrammatic depiction of how wing crack propagation distances in rocks vary with changes in the fracture dip angle, with measurements taken at 5 mm increments, ranging up to 20 mm. The graphical data show that with a set fracture length, the propagation distance of wing cracks initially augments and subsequently diminishes as the fracture dip angle rises. Conversely, with an unvaried dip angle, the propagation distance of wing cracks escalates with an increment in fracture length. Moreover, a prolonged fracture length exacerbates the effect of the fracture dip angle on the propagation distance of wing cracks.

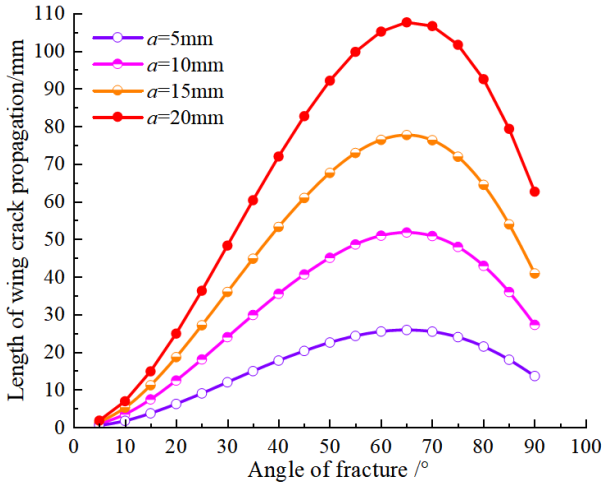

Fig. 11. The influence of fracture length on wing crack propagation length

By inputting various initiation position angles θ into Eqs. (12) and (13), the coefficients b_{11}, b_{12}, and b_{22} for distinct initiation positions were determined. These computed coefficients were subsequently utilized in Eq. (9) to derive the radius of the plastic zone, denoted as (r). At this stage, the stress intensity factors, K_{I} and K_{II}, were found to be dependent solely on the fracture dip angle β. Following this, the calculated parameters were introduced into Eq. (8) to ascertain the displacements, u and v, in the X- and Y-directions for the wing crack. Ultimately, the determined values of u and v were employed in Eq. (7) to compute the wing crack propagation lengths, δ, in rock specimens exhibiting diverse fracture lengths and dip angles.

Fig. 12 depicts the polar coordinate direction angle θ of the wing crack's initiation point in the propagation model, allowing for the adjustment of the wing crack's starting position by varying θ. As θ decreases, the initiation point of the wing crack recedes from the fracture's end. Fig. 12 displays the propagation lengths of wing cracks for different fracture dip angles at θ values of 90°, 80°, 70°, and 60°. Below a 40° fracture dip angle, the initiation position's effect on wing crack length is negligible; above 40°, the peak wing crack length decreases as the initiation point moves further from the fracture end, with the corresponding peak propagation angle also gradually decreasing.

By substituting different θ values into Eq. (5), we calculated the A and B values for different initiation

positions. By substituting different fracture dip angles β into Eq. (1), we solved K_I and K_{II} corresponding to different fracture dip angles. These parameters were then substituted into Eq. (4) to calculate the α_0 for different initiation positions and fracture dip angles. Further, α_0 was substituted into Eq. (6), obtaining the wing crack propagation angle α'.

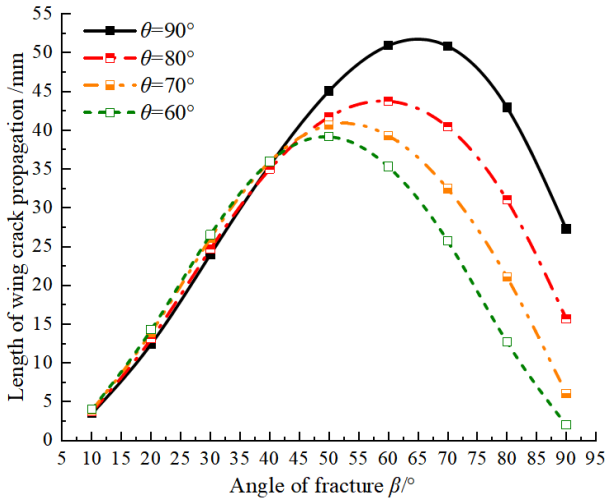

Fig. 12. The Influence of wing crack initiation position on its propagation length

Fig. 13 illustrates the wing crack propagation angles in rock specimens for fracture dip angles ranging from 50° to 90°. The analysis reveals that as the wing crack's initiation point shifts further from the fracture terminus with decreasing θ (from 90°), the propagation angle initially decreases and subsequently increases with an increasing fracture dip angle β when β exceeds 60°, with the inflection point's corresponding β also increasing. When θ equals 60°, the inflection point vanishes, and the propagation angle exhibits a monotonic decrease with β. In summary, the influence of β on the wing crack propagation angle α' diminishes as θ decreases, and at θ = 60°, the propagation angle consistently decreases with β.

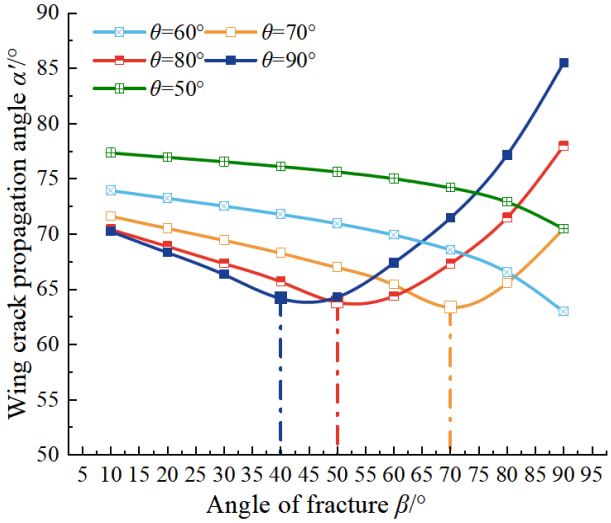

Fig. 13. The influence of wing crack initiation position on its propagation angle

Calculated under different conditions in Fig. 14 were analyzed, and draw the curve can be found that the following rules: when rock fracture dip angle is a fixed value, the rock in the axial load conditions, with the increase of the extended length of crack in the end, the strength of the rock extremum will gradually be reduction. The reduction degree is affected by the final crack propagation length. The longer the final crack propagation length is, the more drastic the reduction degree of rock strength extremum is.

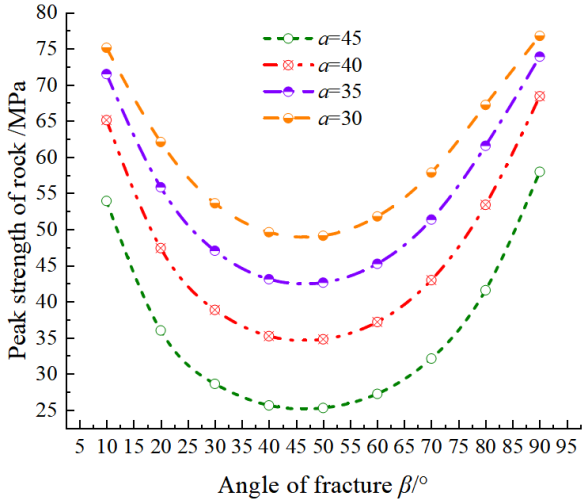

Fig. 14. The influence of fracture length on the peak strength of fractured rock

The extreme strength of rock increases first and then decreases with the gradual increase of fracture inclination angle under the condition of a certain length of fracture propagation. At the same time, the intensity difference between the intensity curves in the figure will also show the same non-monotonic change. The above analysis shows that under the influence of different fracture inclination angles, the peak strength of rock is influenced by the fracture extension length. When the inclination angle of rock fracture is about 45°, the peak strength of rock failure reaches the minimum value, and the longitudinal difference between curves is the largest, that is, the extension length of rock fracture has the most significant influence on the peak strength of rock.

5. Conclusions

The stress-strain characteristics and failure modes of rock under the condition of fracture angle under axial load were studied. The main conclusions are summarized below:

(1) With an increasing fracture dip angle, the rock's closure, peak, and crack initiation stresses escalated swiftly. Simultaneously, the failure mode transitioned from tensile to single-oblique shear, culminating in splitting. Throughout, the wing crack propagation angle first diminished before increasing.

(2) Based on relevant theories of fracture mechanics, a wing crack propagation model for fractured rock was developed to calculate the crack propagation angle and length. A rock strength calculation method that considers the influence of fracture dip angles was proposed combining the M-C strength criterion and the Box-Lucas1 function and validated for its accuracy and reliability. Further, the wing crack propagation factor was incorporated to quantify the progressive failure process of the rock.

(3) As the distance between the wing crack's starting point and the fracture endpoint grows, the fracture dip angle increases, while the wing crack initiation angle initially decreases, then increases, and eventually follows a single downward trend. Concurrently, the wing crack's propagation length shortens, and the dip angle associated with the maximum wing crack propagation length decreases over

time. With a constant fracture inclination, longer fractures decrease the rock's peak strength, with the most pronounced effect occurring at an inclination of 45°.

It is important to study the crack propagation of the fissured wing to understand the failure mechanism of the fissured wing. The subsequent research should focus on the deformation and fracture behavior of rock wing under triaxial stress. In addition, it is important to improve the theoretical model of wing crack propagation in fractured rock to improve the prediction accuracy of the model under various loads.

Acknowledgements

This study was financially supported by the China Postdoctoral Science Foundation (2022M711885), the Science and Technology Development Plan Project of Jilin Province (YDZJ202201ZYTS399), and the Scientific Research Project of Education Department of Jilin Province (JJKH20230139KJ), China.

References

[1] G. S. Esterhuizen, P. L. Tyrna, and M. M. Murphy, "A case study of the collapse of slender pillars affected by through-going discontinuities at a limestone mine in Pennsylvania," *Rock Mech. Rock Eng.*, vol. 52, no. 12, pp. 4941-4952, Sep. 2019.

[2] Z. Aliabadian, M. Sharafisafa, F. Tahmasebinia, and L. Shen, "Experimental and numerical investigations on crack development in 3D printed rock-like specimens with pre-existing flaws," *Eng. Fract. Mech*., vol. 241, pp. 107396, Dec. 2021.

[3] Y. F. Chen and H. Lin, "Consistency analysis of Hoek-Brown and equivalent Mohr-coulomb parameters in calculating slope safety factor," *B. Eng. Geol. Environ.*, vol. 78, no. 6, pp. 4349-4361, Sept. 2019.

[4] M. Saadat and A. Taheri, "A numerical approach to investigate the effects of rock texture on the damage and crack propagation of a pre-cracked granite," *Comput. Geotech*., vol. 111, pp. 89-111, Jul. 2019.

[5] J. H. Yang, S. R. Wang, Y. G. Wang, and C. L. Li, "Analysis of arching mechanism and evolution characteristics of tunnel pressure-arch," *Jordan J. Civil Eng.*, vol. 9, no. 1, pp. 125-132, Jan. 2015.

[6] S. R. Wang, H. Q. Zhang, N. Q. Shen, and H. Y. Cao, "Analysis of deformation and stress characteristics of highway tunnels above mined-out regions," *Chin J. Rock Mech. Eng.*, vol. 28, no. 6, pp. 1144-1151, Jun. 2009.

[7] B. S. Bastola and M. Cai, "Investigation of mechanical properties and crack propagation in pre-cracked marbles using lattice-spring-based synthetic rock mass (LS-SRM) modeling approach," *Comput. Geotech.*, vol. 110, pp. 28-43, Feb. 2019.

[8] M. Saadat and A. Taheri, "Modelling micro-cracking behaviour of pre-cracked granite using grain-based distinct element model," *Rock Mech. Rock Eng.*, vol. 52, no. 11, pp. 4669-4692, May. 2019.

[9] S. R. Wang, Y. H. Wang, J. Gong, Z. L. Wang, Q. X. Huang, and F. L. Kong, "Failure mechanism and constitutive relation for an anchorage segment of an anchor cable under pull-out loading," *Acta Mech.*, vol. 231, no. 8, pp. 3305-3317, Jul. 2020.

[10] S. Laarmagnat, M. D. Roches, and L. F. Daigle, "Continuous porosity characterization: Metric-scale intervals in heterogeneous sedimentary rocks using medical CT-scanner," *Mar. Petrol. Geol.*, vol. 109, pp. 361-380, Jun. 2019.

[11] S. Zafar, A. Hedayat, and O. Moradian, "Micromechanics of fracture propagation during multistage stress relaxation and creep in brittle rocks," *Rock Mech. Rock Eng.*, vol. 55, no. 12, pp. 7611-7627, Sep. 2022.

[12] L. N. Y. Wong and Q. Xiong, "A method for multiscale interpretation of fracture processes in Carrara marble specimen containing a single flaw under uniaxial compression," *J. Geophys Res-sol. Ea.,* vol. 123, no. 8, pp. 6459-6490, Jul. 2018.

[13] S. Q. Yang and H. W. Jing, "Strength failure and crack coalescence behavior of brittle sandstone samples containing a single fissure under uniaxial compression," *Int. J. Fract.*, vol. 168, pp. 227-250, Dec. 2011.

[14] M. Naderloo, M. Moosavi, and A. Ahmadi, "Using acoustic emission technique to monitor damage progress around joints in brittle materials," *Theor. Appl. Fract. Mech*., vol. 104, pp. 102368, Oct. 2019.

[15] Y. Bernabé and M. Pec, "Brittle creep and failure: a reformulation of the wing crack model," *J. Geophys Res-sol. Ea.,* vol. 127, no. 9, pp. e2022JB024610, Sep. 2022.

[16] J. Duriez, L. Scholtès, and F. V. Donzé, "Micromechanics of wing crack propagation for different flaw properties," *Eng. Fract. Mech.*, vol. 153, pp. 378-398, Jan. 2016.

[17] S. Lee, J. E. Reber, and N. W. Hayman, "Investigation of wing crack formation with a combined phase-field and experimental approach," *Geophys. Res. Lett.*, vol. 43, pp. 7946-7952, Aug. 2016.

[18] G. Pepe, S. Mineo, G. Pappalardo, and A. Cevasco, "Relation between crack initiation-damage stress thresholds and failure strength of intact rock," *B. Eng. Geol. Environ.*, vol. 77, pp. 709-724, Oct. 2018.

[19] H. Mohammadi and S. Pietruszczak, "Description of damage process in fractured rocks," *Int. J. Rock Mech. Min. Sci.*, vol. 113, pp. 295-302, Jan. 2019.

[20] H. Dang-Trung, E. Keilegavlen, and I. Berre, "Numerical modeling of wing crack propagation accounting for fracture contact mechanics," *Int. J. Solid Struct.*, vol. 204, pp. 233-247, Sep. 2020.

[21] S. Mohanty, and R. R. Das, "Influence of polymeric resin-infilling on onset and fracture growth along wing trajectory in open-flawed sandstone specimen," *Theor. Appl. Fract. Mech.*, vol. 125, pp. 103836, Jun. 2023.

[22] H. Yang, H. Lin, Y. Chen, Y. Wang, and W. Zhao, "Influence of wing crack propagation on the failure process and strength of fractured specimens," *B. Eng. Geol. Environ.*, vol. 81, no. 1, pp. 71, Jan. 2022.

[23] K. Cheng, T. D. Xia, R. Z. Liang, S. Y. Feng, R. Q. Xu, and X. G. Wang, "Vertical response analysis of adjacent existing single pile under tunneling," *Chin. J. Geotech. Eng.*, vol. 40, pp. 42-46, Oct. 2018.

[24] Z. Wang, X. Xie, and J. Wang, "A new nonlinear method for vertical settlement prediction of a single pile and pile groups in layered soils," *Comput. Geotech.*, vol. 45, pp. 118-126, Sep. 2012.

[25] Q. F. Guo, X. Wu, M. F. Cai, X. Xi, F. H. Ren, and S. J. Miao, "Experiment on the strength characteristics and failure modes of granite with pre-existing cracks," *Chin. J. Eng. Sci.*, vol. 41, pp. 43-52, Jan. 2019.

[26] S. Q. Yang, W. L. Tian, P. G. Ranjith, X. R. Liu, M. Chen, and W. Cai, "Three-dimensional failure behavior and cracking mechanism of rectangular solid sandstone containing a single fissure under triaxial compression," *Rock Mech. Bull.*, vol. 100008, pp. 1-23, Oct. 2022.

[27] Y. Q. Wang, K. Peng, X. Y. Shang, L. P. Li, Y. Wu, and L. Long, "Experimental and numerical simulation study of crack coalescence modes and microcrack propagation law of fissured sandstone under uniaxial compression," *Theor. Appl. Fract. Mech.*, vol. 115, pp. 103060, Oct. 2021.

[28] T. L. Xiao, M. Huang, and M. Gao, "Experimental study of the mechanical characteristics of a rock-like material containing a preexisting fissure under loading and unloading triaxial compression," *Adv. Civ. Eng.*, vol. 2020, no. 1, Art. no. 9374352, Feb. 2020.